Laser powder bed fusion of 17–4 PH stainless steel

Sabooni, S.; Chabok, A.; Feng, S. C.; Blaauw, H.; Pijper, T. C.; Yang, H. J.; Pei, Y. T.

Published in:
Additive Manufacturing

DOI:
10.1016/j.addma.2021.102176

Publication date:
2021

Additive Manufacturing 46 (2021) 102176

Contents lists available at ScienceDirect

Additive Manufacturing

journal homepage: www.elsevier.com/locate/addma

Research Paper

Laser powder bed fusion of 17–4 PH stainless steel: A comparative study on the effect of heat treatment on the microstructure evolution and mechanical properties

S. Sabooni [a], A. Chabok [a], S.C. Feng [a,e], H. Blaauw [b], T.C. Pijper [b,c], H.J. Yang [d], Y.T. Pei [a,*]

[a] Department of Advanced Production Engineering, Engineering and Technology Institute Groningen, University of Groningen, Nijenborgh 4, 9747 AG Groningen, The Netherlands
[b] Philips Personal Care, Oliemolenstraat 5, 9203 ZN Drachten, The Netherlands
[c] Innovation Cluster Drachten, Nipkowlaan 5, 9207 JA Drachten, The Netherlands
[d] Shi-changxu Innovation Center for Advanced Materials, Institute of Metal Research, Chinese Academy of Sciences, 72 Wenhua Road, Shenyang 110016, China
[e] School of Mechanical Engineering, University of Science and Technology Beijing, Beijing 100083, China

ARTICLE INFO

Keywords:
Laser powder bed fusion
17-4 PH stainless steel
Post-process heat treatment
Age hardening
Reverted austenite

ABSTRACT

17–4 PH (precipitation hardening) stainless steel is commonly used for the fabrication of complicated molds with conformal cooling channels using laser powder bed fusion process (L-PBF). However, their microstructure in the as-printed condition varies notably with the chemical composition of the feedstock powder, resulting in different age-hardening behavior. In the present investigation, 17–4 PH stainless steel components were fabricated by L-PBF from two different feedstock powders, and subsequently subjected to different combinations of post-process heat treatments. It was observed that the microstructure in as-printed conditions could be almost fully martensitic or ferritic, depending on the ratio of Cr_{eq}/Ni_{eq} of the feedstock powder. Aging treatment at 480 °C improved the yield and ultimate tensile strengths of the as-printed components. However, specimens with martensitic structures exhibited accelerated age-hardening response compared with the ferritic specimens due to the higher lattice distortion and dislocation accumulation, resulting in the "dislocation pipe diffusion mechanism". It was also found that the martensitic structures were highly susceptible to the formation of reverted austenite during direct aging treatment, where 19.5% of austenite phase appeared in the microstructure after 15 h of direct aging. Higher fractions of reverted austenite activates the transformation induced plasticity and improves the ductility of heat treated specimens. The results of the present study can be used to tailor the microstructure of the L-PBF printed 17–4 PH stainless steel by post-process heat treatments to achieve a good combination of mechanical properties.

1. Introduction

17–4 PH stainless steel is a precipitation hardening steel that combines good corrosion resistance, high strength and toughness [1]. Post-process heat treatment is often essential for 17–4 PH stainless steel to meet the requirements of mechanical properties and corrosion resistance [1,2]. The optimal hardness and strength are usually achieved after an aging treatment at the temperature range of 480–620 °C through the uniform precipitation of nanometric copper-rich precipitates [3,4]. The actual aging time depends on the aging temperature ranging from a few minutes to hours. The application of the 17–4 PH stainless steel covers various industries including marine, chemical and power generation [1–5].

One of the growing applications of the 17–4 PH stainless steel is the fabrication of injection molds with high strength and wear resistance. The performance of the injection molds can be remarkably improved by using the conformal cooling channel design. It effectively reduces the cooling time and the inhomogeneous heat distribution [6], consequently influences both the rate of the process and the quality of the products. Laser powder bed fusion (L-PBF), also commonly referred to selective laser melting (SLM), has been attracted a lot of attention in the past few years for the fabrication of conformal cooling molds [7,8]. L-PBF is a type of additive manufacturing process in which a focused laser beam selectively fuses a metal powder bed to build up a three-dimensional

* Corresponding author.
E-mail address: y.pei@rug.nl (Y.T. Pei).

https://doi.org/10.1016/j.addma.2021.102176
Received 27 April 2021; Received in revised form 5 June 2021; Accepted 7 July 2021
Available online 8 July 2021

Table 1
Chemical composition (wt%) of the commercial feedstock 17–4 PH powders.

Powder	C	Cr	Cu	Ni	Mn	N	Nb	Si	Fe	Cr_{eq}/Ni_{eq}
Powder A (SLM Solution)	0.07	17.7	3.3	4.2	1	0.1	0.14	0.07	balance	1.75
Powder B (LPW Technology)	0.01	15.6	3.89	4.03	0.24	0.01	0.33	0.29	balance	2.73

Table 2
Optimized process parameters for L-PBF of 17–4 PH stainless steel.

Parameters	Interior region	Border region
Laser power (W)	200	100
Scan speed (mm/s)	820	400
Hatch spacing (μm)	108	N/A
Layer thickness (μm)	30	N/A
Scan strategy	Stripes, 10 mm wide	N/A
Hatch rotation angle	33° after each layer	N/A

(3D) metallic part layer-by-layer [9,10]. The L-PBF process is capable of creating complex and near net shape components with relatively high densities and mechanical properties comparable or even better than the wrought counterparts. Consequently, it has become a preferred manufacturing technique for the fabrication of complicated mold designs with conformal cooling channels that were previously challenging (or even impossible) to manufacture via conventional manufacturing techniques.

Although the commercial wrought 17–4 PH stainless steel exhibits a martensitic structure, a wide range of contradictory microstructures have been reported in additively manufactured 17–4 PH steel [11]. A dominant martensitic structure with small amounts of retained austenite (RA) was reported for 17–4 PH stainless steel L-PBF printed under an argon (Ar) processing atmosphere while a mixture of martensite and austenite phases (50–75% of austenite at different cross sections) was formed under an N_2 processing atmosphere [12]. A predominant martensitic microstructure with 7% and 3% RA was reported for the L-PBF printed 17–4 PH stainless steel in vertical and horizontal planes, respectively. The difference of the microstructure in vertical and horizontal planes was related to the variation of distinct thermal history during fabrication [13]. A coarse grain ferritic structure elongated across the building direction was noticed for the L-PBF printed 17–4 PH stainless steel by Alnajjar et al. [14,15]. Nezhadfar et al. [16] also reported the formation of a ferritic microstructure for both N_2 atomized and Ar atomized 17–4 PH stainless steel powders. The grain structure of the N_2 atomized powder seemed to be finer and contained the islands of the equiaxed ultrafine grains, while the Ar atomized powder exhibited coarse and elongated grains after laser printing [16]. The very high cooling rates associated with the L-PBF process might be a potential reason for the formation of non-equilibrium phases during solidification depending on the precise chemical composition of the feedstock powder and the thermal history of the specimens.

So far, the lack of profound understanding about the microstructure of additive manufactured 17–4 PH stainless steel and the influence of the post-process heat treatment is sensible. The current investigation focuses on the effect of the chemical composition of the feedstock powder and the role of post-process heat treatments on the solidification mode, microstructure and mechanical properties of L-PBF printed 17–4 PH stainless steel.

2. Materials and methods

Two commercial Ar atomized 17–4 PH stainless steel powders from two different manufacturers (SLM Solution, Germany and LPW Technology, UK) were used. The elemental composition of the feedstock powders is summarized in Table 1. Wrought 17–4 PH steel in the form of a 3 mm diameter rod bar (solution annealed condition) is also studied for comparison.

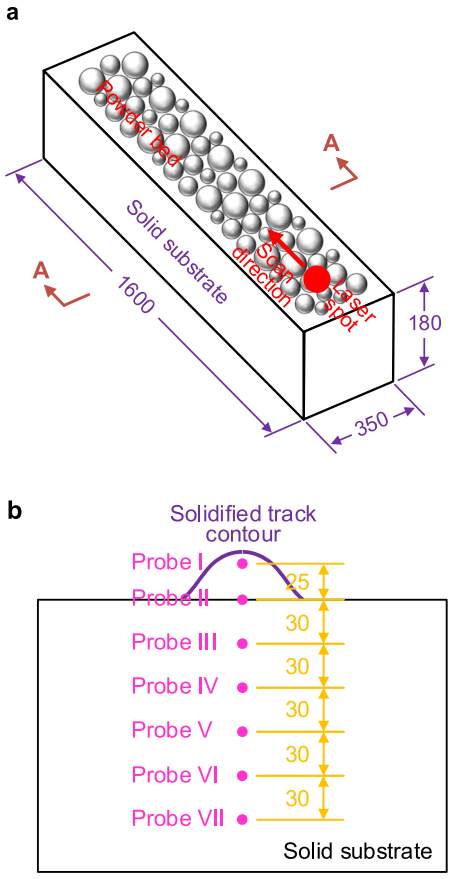

Fig. 1. Schematic of (a) geometry of the simulation model, (b) A-A cross-section presenting the locations of point probes for recording temperature history (unit: μm).

The SLM 125 HL and SLM 280 HL machines (SLM Solution, Germany) were used to conduct the L-PBF. The two machines used the same laser system (400 W fiber laser and scanner) and the main difference was the maximum dimensions of the printed samples (125 mm versus 280 mm). Optimized process parameters were used for the fabrication of all the specimens according to Table 2. All the processing steps were conducted in a protective Ar atmosphere to avoid oxidation. The temperature of the build plate was set to 100 °C for all the experiments. Cubic samples with the dimension of 10 mm were printed for microstructural analysis. Tensile specimens were printed according to the ASTMD-638–IV standard, with the gauge being dimensioned at 33 (length) × 6 (width) × 1.5 (thickness) mm that was polished to 1.0 mm thickness for tensile test.

The as-printed samples were subjected to different combinations of post-process heat treatments. Solution annealing (SA) was performed at 1040 °C for 0.5 h. Aging was performed at 480 °C for different durations ranging from 0.5 h to the maximum of 24 h. Hot isostatic pressing (HIP) was also conducted at 1150 °C for 4 h at an isostatic pressure of 100 MPa. The preparation of metallographic specimens was carried out using the standard procedures. The as-printed and heat treated specimens were chemically etched by modified Fry's reagent (1 g $CuCl_2$, 50 ml HCl, 150 ml H_2O, 50 ml HNO_3) to reveal the microstructures.

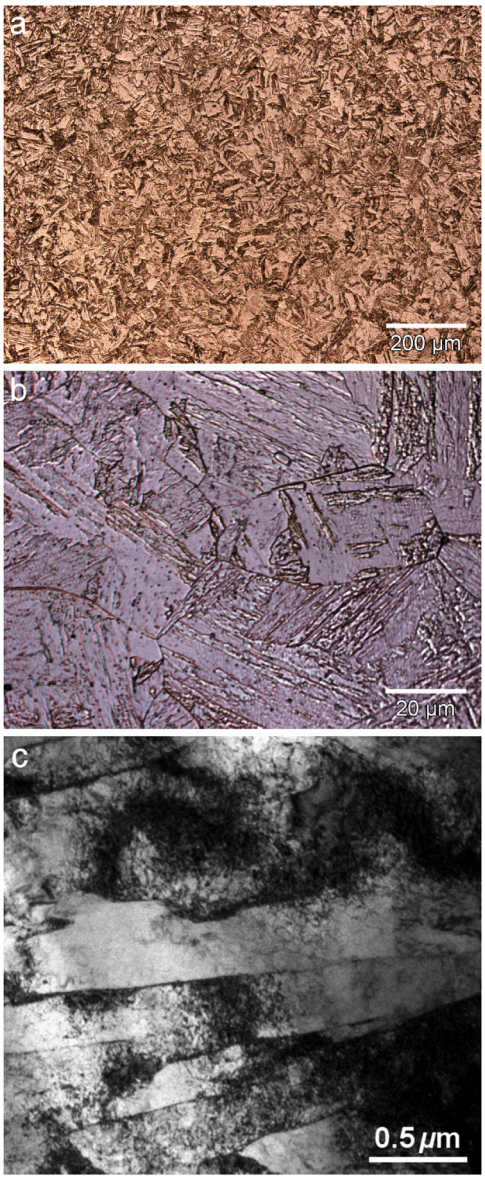

Fig. 2. Optical (a, b) and TEM (c) micrographs of the wrought 17–4 PH stainless steel.

Microstructural characterization was performed using an optical microscope (Olympus VANOX-T) and scanning electron microscope (SEM, Philips ESEM-XL30 FEG). Microstructures of the samples were further characterized using transmission electron microscopy (TEM, FEI Tecnai F30) operated at 300 kV. For TEM observations, a ø3 mm disks of 0.5 mm thickness was sliced from the as-received samples by spark-cutting and then mechanically reduced to ~50 µm thick, followed by twin-jet electro-polishing. Orientation imaging microscopy (OIM) analysis was carried out with a scan step size of 0.08–0.2 µm depending on the desired resolution using an electron backscattered diffraction (EBSD) system (EDAX, USA) installed in the SEM operated at 25 kV. Microhardness measurements were performed by a CSM Revetest scratch/microhardness tester at the normal load of 5 N and dwell time of 10 s. A minimum number of 15 indentations were carried out for each sample. Tensile properties of the as-printed and heat treated specimens were evaluated according to the ASTMD-638–IV standard. Five tensile specimens were tested for each metallurgical condition. The obtained data was analyzed to plot the stress-strain curves and measure the 0.2% proof yield stress, ultimate tensile strength (UTS) and the elongation to failure.

Computational fluid dynamics (CFD) simulation was conducted using the commercial software Flow-3D® v11.2 to investigate the temperature history and the cooling rate of the melt pool in the L-PBF process. In the simulation, a track was printed on a solid substrate using the same process parameters as applied in the experiments. The model geometry is schematically illustrated in Fig. 1a. A cross-section (A-A cross-section in Fig. 1a) was selected along the middle of the track on which 7 point-probes were set to record the local temperature history at different Z-coordinates during the printing process. The locations of these point-probes on A-A cross-section are shown in Fig. 1b. Probe II was located exactly on the top surface of the solid substrate. Except for probe I, the distance of each two adjacent probes was 30 µm, which was equal to the layer thickness used for the L-PBF process. Thus, each probe was located on the top of the corresponding previous layer, and exposed to the maximum temperature of the layer during melting and solidification. During the L-PBF process, the height of the melt pool might change over time due to the driving of the transient gradient of surface tension. To ensure the probe was located always on the melt pool/solidified track during the process, the location of Probe I was selected at the height of 25 µm above the top surface of the solid substrate. In the L-PBF experiments, a 30 s cooling window was used to minimize the heat accumulation and ensure sufficient cooling before the printing of the next layer. It was therefore reasonable to assume that the previous layer was cooled down to surrounding temperature (~ 100 °C) before starting the printing of the next layer. Consequently, although the probes collected temperature data from seven different points, the temperature profiles recorded by the probes could also represent the temperature history of a specific point during 7 successive heating/cooling cycles. More detailed information about the CFD simulation can be found in [17].

3. Results and discussion

3.1. Microstructure of wrought 17–4 PH stainless steel

The optical micrographs of the wrought steel (Fig. 2a–b) reveal a well-defined typical lath-type martensitic structure inside distinct prior austenite grains. A TEM micrograph of the wrought 17–4 PH steel (Fig. 2c) also confirms the presence of lath-type martensite with an average thickness of ~ 250 nm. The microhardness of the wrought material was measured as 331 ± 6 HV.

3.2. Microstructure of the L-PBF printed 17–4 PH stainless steel

Different cross sections of the as-printed components fabricated with powder A and B, perpendicular and parallel to the building direction, are carefully investigated and the corresponding EBSD and SEM micrographs are presented in Figs. 3 and 4. The as-printed component from "powder A" exhibits a fine martensitic microstructure with ~ 1.5% of RA (Fig. 3a and b), while a dominant ferritic structure containing large ferrite grains is detected in the as-printed specimens from "powder B" (Fig. 3c and d). The average depth of the melt pools was measured as ~ 90 µm for both samples. The columnar ferrite grains in Fig. 3d can reach a maximum length of ~150 micrometers, thus extending over a few layers of melted and solidified powder. It means that the freshly solidifying grains nucleate and grow on the previously solidified ferrite grains by adopting their orientation, indicating epitaxial growth. The microhardness of the as-printed components with martensitic and ferritic microstructures is measured as 350 ± 13.2 HV and 303 ± 4.5 HV, respectively. SEM micrographs presented in Fig. 4 confirm a very small fraction of the retained austenite in the as-printed condition.

The metallurgical evolution of this steel was analyzed upon solidification and cooling in order to investigate the reasons for the presence of different microstructures in the as-printed condition. Under equilibrium cooling condition, 17–4 PH stainless steel usually solidifies as primary delta ferrite from liquid state [18]. The delta-ferrite phase subsequently transforms to austenite to a great extent during cooling

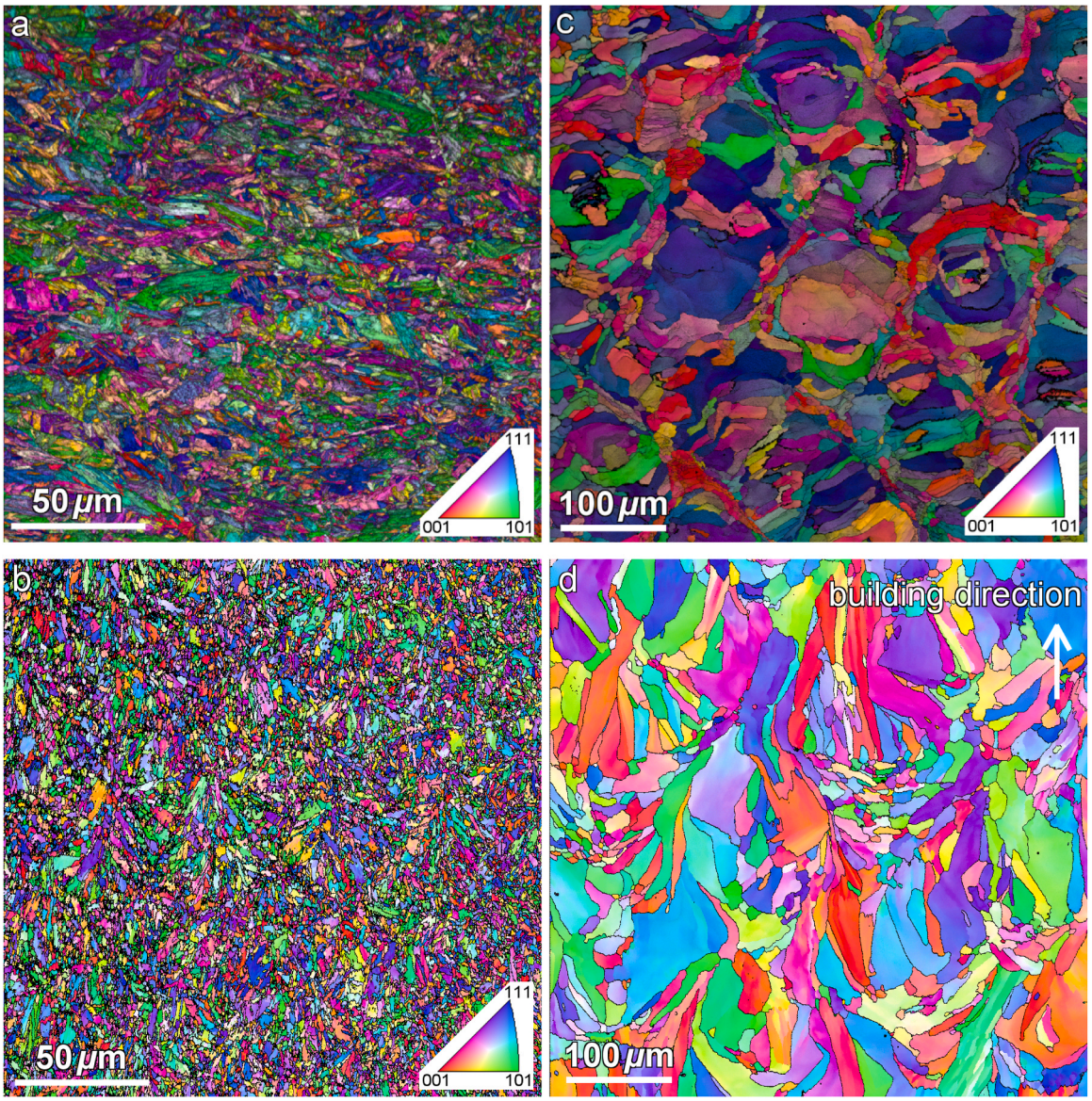

Fig. 3. EBSD micrographs of the as-printed 17–4 PH stainless steel fabricated with "powder A" (a, b) and "powder B" (c, d) on two different cross sections: (a, c) perpendicular to the building direction, and (b, d) parallel to the building direction.

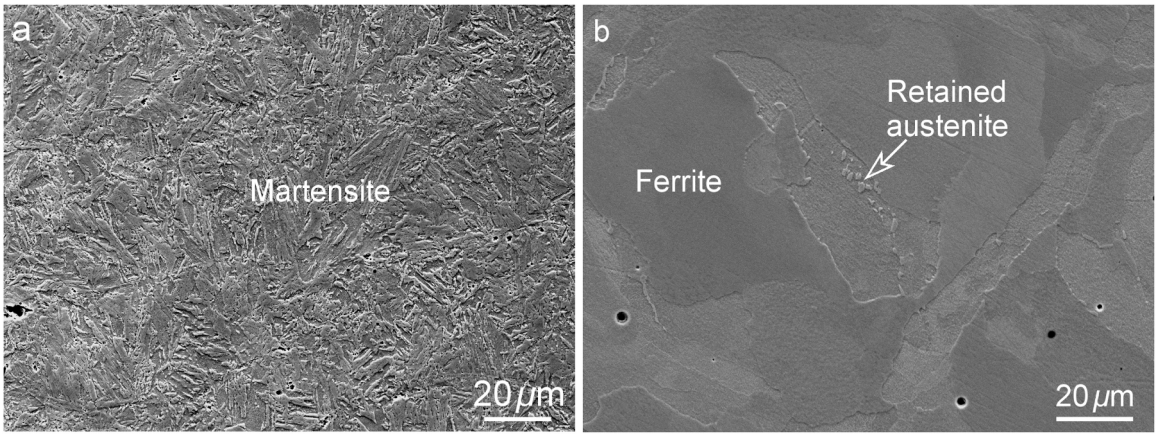

Fig. 4. Microstructure of the as-printed 17–4PH stainless steel fabricated with "powder A" (a) and "powder B" (b).

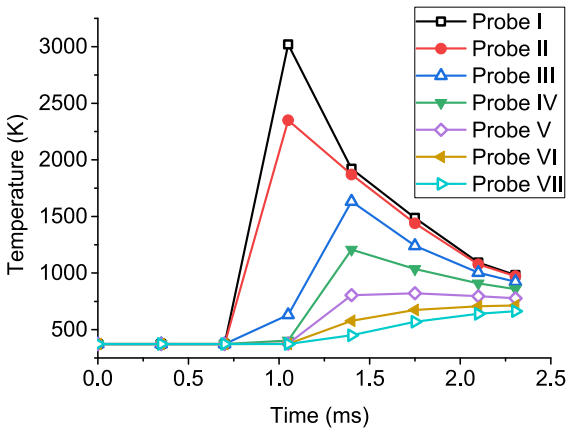

Fig. 5. Simulated temperature history of the probes located at the cross section of the L-PBF 17–4 PH stainless steel sample.

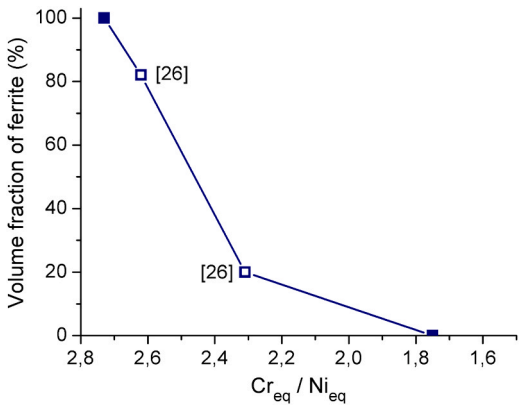

Fig. 6. Dependency of the volume fraction of delta ferrite in the final microstructure of L-PBF printed 17–4 PH stainless steel as a function of Cr_{eq}/Ni_{eq}.

due to the solid-state diffusion. The austenite to martensite transformation is the following step at the temperature range of 132 °C until room temperature [18]. It explains the predominant martensitic structure of the wrought 17–4 PH stainless steel (Fig. 2). The ratio of Cr_{eq}/Ni_{eq} plays a crucial role in the solidification mechanism/mode of stainless steels [19]. Considering the presence of different alloying elements in the chemical composition of the investigated steel, the following equations were used to determine the chromium equivalent (Cr_{eq}) and nickel equivalent (Ni_{eq}) of different feedstock powders [20]:

$$Cr_{eq}\ (wt\%) = Cr + 2(Si) + 1.5(Mo) + 5(V) + 5.5(Al) + 1.75(Nb) + 1.5(Ti) + 0.75(W) \quad (1)$$

$$Ni_{eq}\ (wt\%) = Ni + (Co) + 0.5(Mn) + 0.3(Cu) + 25(N) + 30(C) \quad (2)$$

The ratio of Cr_{eq}/Ni_{eq} was calculated as 1.75 and 2.73 for powder A and B, respectively. Under equilibrium conditions, if the ratio of Cr_{eq}/Ni_{eq} is higher than 1.5, which is the case for both powders, the first solidified phase is δ-ferrite instead of austenite [19]. This critical value of Cr_{eq}/Ni_{eq} increases with increasing the cooling rate and has been reported to be ~ 1.7 in pulsed laser welding [21,22]. The simulated temperature history of the probes located at the cross-section of the printed specimens is illustrated in Fig. 5. According to the simulation results, the cooling rate is calculated around 10^6 K/s for the L-PBF parameters used in this study, which is in the same order as reported earlier in the literature. The cooling rate was estimated to be ~ 1.7×10^6 K/s for the L-PBF printing of 316 L stainless steel [23], and similar values in the range of 10^5–10^7 K/s reported in [24]. This is much higher than the cooling rates in most common manufacturing techniques such as casting (10^0–10^2 K/s), arc welding (10^1–10^3 K/s) and laser welding (10^2–10^6 K/s) [25]. Therefore, the critical value of the Cr_{eq}/Ni_{eq} ratio in our experimental condition is certainly higher than 1.7, considering the higher cooling rate of L-PBF process compared with pulse laser welding.

The solidification mode of the as-printed specimen with "powder A" is recognized as austenitic. The austenite finally transformed to martensite and therefore martensite is the dominant phase at room temperature. However, in the case of the "powder B", whose solidification occurred in δ-ferrite mode, the transformation of δ-ferrite to austenite (below the solidus temperature) might not be valid anymore due to the high cooling rate of the L-PBF. If the cooling rate is high enough, the delta ferrite phase will pass the austenite stability region without transformation to austenite and therefore the ferrite phase remains dominant at room temperature. However, in the case of a low cooling rate, a small or large fraction of delta ferrite may transform to austenite during cooling. The transformation of delta ferrite to austenite during cooling cycle depends on the time that ferrite passes through the austenite stability region (ferrite instability region) [26]. Longer cooling time in this region causes more transformation to austenite and therefore less residual ferrite. It has been reported that the passing time through the austenite stability region depends on the chemical composition and increases with decreasing the ratio of Cr_{eq}/Ni_{eq} [26]. Fig. 6 demonstrates the volume fraction of the remaining ferrite phase in the final microstructure of the as-printed 17–4 PH stainless steel versus the ratio of Cr_{eq}/Ni_{eq}. A couple of data points are adopted from reference [26]. As seen the volume fraction of the ferrite phase in the L-PBF printed 17–4 PH stainless steel decreases with decreasing the ratio of Cr_{eq}/Ni_{eq}. Therefore, in the case of "powder B", where the ratio of Cr_{eq}/Ni_{eq} is high enough (2.73), no austenite can form below the solidus temperature and δ-ferrite phase is the only stable phase at the room temperature.

3.3. *The effect of post-process heat treatments on the microstructure and mechanical properties of the L-PBF printed 17–4 PH stainless steel*

The as-printed specimen with martensitic structure (printed with "powder A") were subjected to different combinations of post-process heat treatments (direct aging, HIP + aging, SA + aging, HIP + SA + aging). The aging duration for all of these samples was set to 1 h. The dominant microstructure of the post-process heat treated samples is still martensite. However, a much coarser lath structure is detected in the specimens after SA and HIP treatments (see Fig. 7). To address this phenomenon, the parent austenite grains of the martensitic structure is reconstructed and presented in Fig. 7. There are different well-established orientation relationships (ORs) between the parent austenite and transformed martensite phases. These ORs are based on reducing the crystallographic mismatch between the parent and product phases leading to a minimized transformation strain energy. It is widely accepted that the OR for steels with a low carbon content can be described by the Kurdjumov–Sachs (K-S) orientation relationship. According to this OR, a single parent austenite grain is transformed to 24 crystallographic variants of martensite where the closed-packed planes and directions of martensite are parallel to those of austenite [27]. In the current study, the K-S orientation relationship was also confirmed by comparing the experimental pole figure of martensite variants inside one single parent austenite grain and ideal pole figure for K-S relationship. To reconstruct large-scale parent austenite maps assuming K-S OR without a need for retained austenite, the ARPGE program code [28] written in Python was used. The reconstruction was done using nucleation/growth algorithm during which three neighbor martensite variants were selected and their misorientation were compared with the theoretical operators with low tolerance angle. If confirmed, these three variants were considered as a nucleus of prior austenite which could grow according to the same procedure but with a higher tolerance angle. The grain size of the parent austenite for the direct aged condition was measured as 6.5 ± 1 μm. In contrast, the grain size of the parent

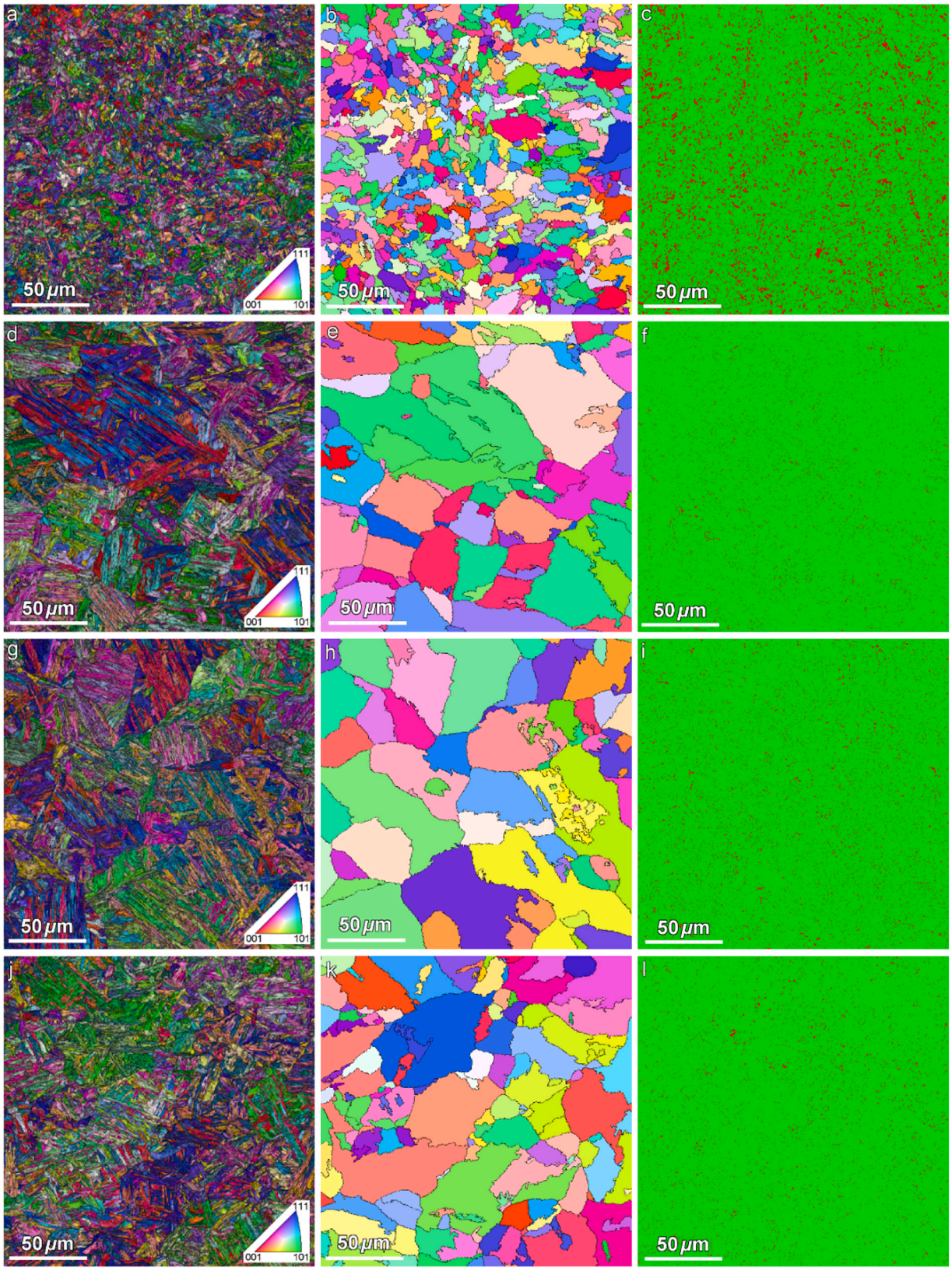

Fig. 7. IQ + IPF (left column), parent austenite grain maps (middle column) and phase maps (right column, green color = martensite, red color = austenite) of the post-process heat treated 17–4 PH stainless steel: (a-c) direct aged, (d-f) HIP + aging, (g-i) SA + Aging, and (j-l) HIP + SA + aging (all sample were printed with "powder A").

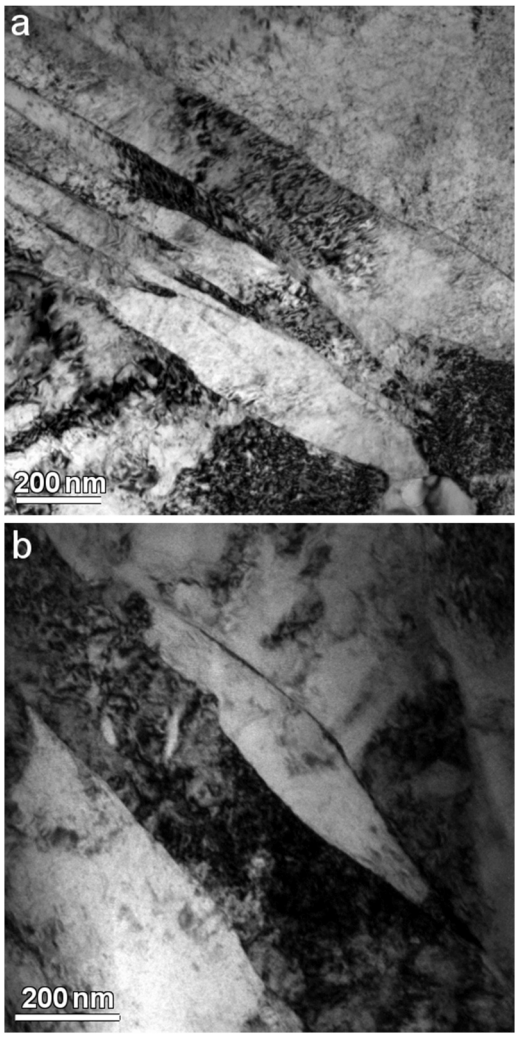

Fig. 8. TEM micrographs of the post-process heat treated 17–4 PH stainless steel: (a) direct aging and (b) HIP + aging (printed with "powder A").

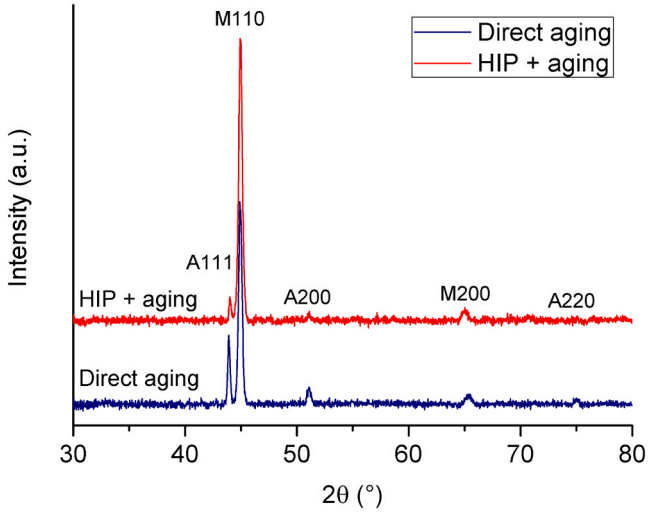

Fig. 9. XRD patterns of the post-process heat treated 17–4 PH stainless steel printed with "powder A".

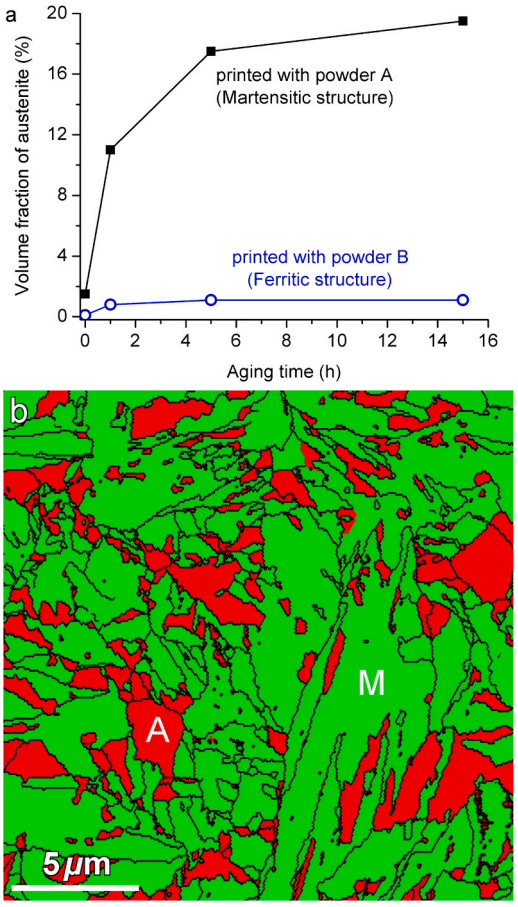

Fig. 10. (a) Volume fraction of reverted austenite as a function of aging time for "direct aging" condition, (b) phase map (green color = martensite, red color = austenite) of the 15 h direct aged specimen printed with "powder A".

austenite substantially increased to ~ 18.2 ± 3.5 μm and 19 ± 5.2 μm after the "HIP + aging" and "SA + aging" treatments. The larger grain size of the parent austenite subsequently resulted in the coarser martensitic microstructure by phase transformation. The TEM micrographs of the martensite laths after "direct aging" and "HIP + aging" treatments confirm the coarsening of martensite laths after HIP processing (Fig. 8).

EBSD analysis showed that the volume fraction of the retained austenite phase for the "SA + aging", "HIP + aging" and "HIP + SA + aging" conditions increases slightly compared with the as-printed specimen but remains in the range of 2.0–3.5%. However, a much larger fraction of reverted austenite is detected after "direct aging" (11%). This is also evident from the XRD patterns of the specimens after "direct aging" and "HIP + aging" treatments (see Fig. 9). It has been reported that localized segregation of the austenite stabilizing elements such as N and Ni at the boundaries of prior austenite grains and martensite laths are responsible for the formation of reverted austenite during subsequent aging of 17–4 PH stainless steel [4,29]. SA, HIP or combination of them can effectively homogenize the distribution of these elements and thus suppress/eliminate the formation of reverted austenite during aging treatment to a great extent. However, the already segregated elements at the boundaries of the as-printed sample provide an appropriate environment for the genesis of reverted austenite during direct aging. It is worth to mention that a two-phase structure consisting of martensite and austenite may have both beneficial and detrimental effects on the mechanical properties and corrosion resistance of the steel, depending on the intended application. For instance, a higher fraction of austenite may encourage the formation of strain-induced martensite, resulting in a delayed onset of localized plastic

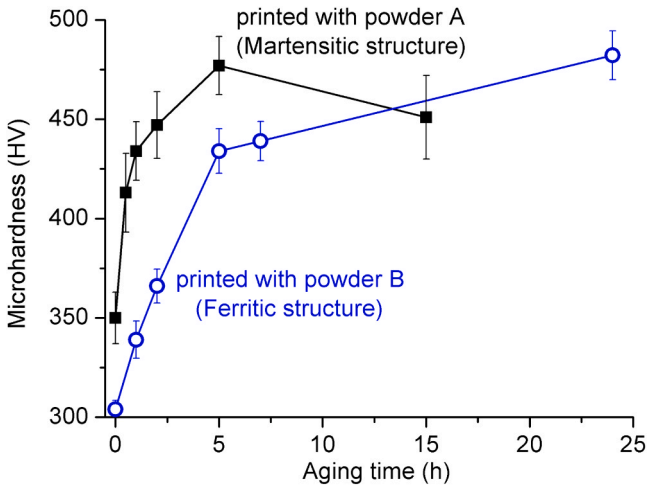

Fig. 11. Microhardness variations of the "direct aged" specimens as a function of aging time at 480 °C.

deformation and improved work hardening behavior [30,31]. On the other hand, it may jeopardize the abrasive wear behavior of the components due to the higher constitution of the softer phase.

The evolution of reverted austenite as a function of aging duration at 480 °C is depicted in Fig. 10a for the "direct aging" condition. As seen, the printed specimens with ferritic and martensitic microstructures exhibit different behavior in terms of austenite reversion during direct aging. The ferritic structure is highly resistant against the austenite reversion where only 1.1% austenite is formed after direct aging for 15 h. However, the volume fraction of reverted austenite increases substantially from 1.5% to 11% only after 1 h aging in the martensitic specimens. The rate of austenite reversion decreases subsequently, where 17.5% and 19.5% of reverted austenite is detected after 5 h and 15 h direct aging, respectively. The observations of the present investigation are in line with [29], where the formation of reverted austenite was reported to take place right from the initial stages of the aging. The phase map of the 15 h "direct aged" specimen (Fig. 10b) confirms that the reverted austenite is mostly nucleated and grown at the grain boundaries of martensite laths [27].

Fig. 11 shows the variations of the microhardness of "direct aged" specimens as a function of aging time for both as-printed samples. Explicit distinctions can be made between the hardening behavior of the martensitic and ferritic microstructures during direct aging treatment. The microhardness of the martensitic microstructure increases gradually with aging time, where the peak hardness of 477 ± 16.8 HV is achieved after 5 h aging. The microhardness decreases subsequently to 451 ± 21 HV after 15 h aging. However, the ferritic microstructure demonstrates a delayed hardening behavior and a peak hardness of 482 ± 12.3 HV is achieved after 24 h direct aging. The increased hardness of 17–4 PH stainless steel upon aging is related to the formation of nanosized ε-Cu-rich precipitates [32–34]. Although the size of such Cu-rich precipitates was reported even as fine as 1 nm after aging time of 1 h [32], the majority of literature reported a size of 10–20 nm at the optimal aging conditions [33,34]. These precipitates act as obstacles and hinder the movement of dislocations through the well-known Orowan mechanism [35]. The decrease of the hardness of martensitic microstructure with prolonged aging times can be ascribed to (i) the recovery of dislocations, (ii) coarsening of Cu-rich precipitates and (iii) the formation of reverted austenite [35]. The hardness of the aged specimens may even drop to values lower than the hardness of the solution annealed condition after prolonged aging at temperatures above 595 °C [36].

The accelerated age-hardening response of the martensitic microstructure can be explained by the enhanced diffusivity of precipitation elements due to the higher fractions of grain boundaries and also higher dislocation density of the lath-type martensite. Kernel average misorientation (KAM) graphs of the as-printed specimens are presented in Fig. 12. KAM quantifies the average local misorientation around the measurement point with respect to its nearest neighbors and thus can be utilized to evaluate the lattice distortion and also dislocation accumulation. A higher KAM value denotes higher stored energy in the structure and subsequently higher driving force for precipitation. The kernel average misorientation graphs confirm higher lattice distortion of the martensitic microstructure, resulting in less activation energy for diffusion. It has been also reported that the martensitic structure of 17–4 PH stainless steel contains a very high dislocation density in the as-printed or solution annealed conditions [37], which results in the "dislocation pipe diffusion mechanism" and consequently faster formation of the nanometric Cu-rich precipitates.

Typical stress-strain curves of the as-printed and post-process heat treated components (printed with "powder A") as well as their yield strength, ultimate tensile strength and the elongation to failure are

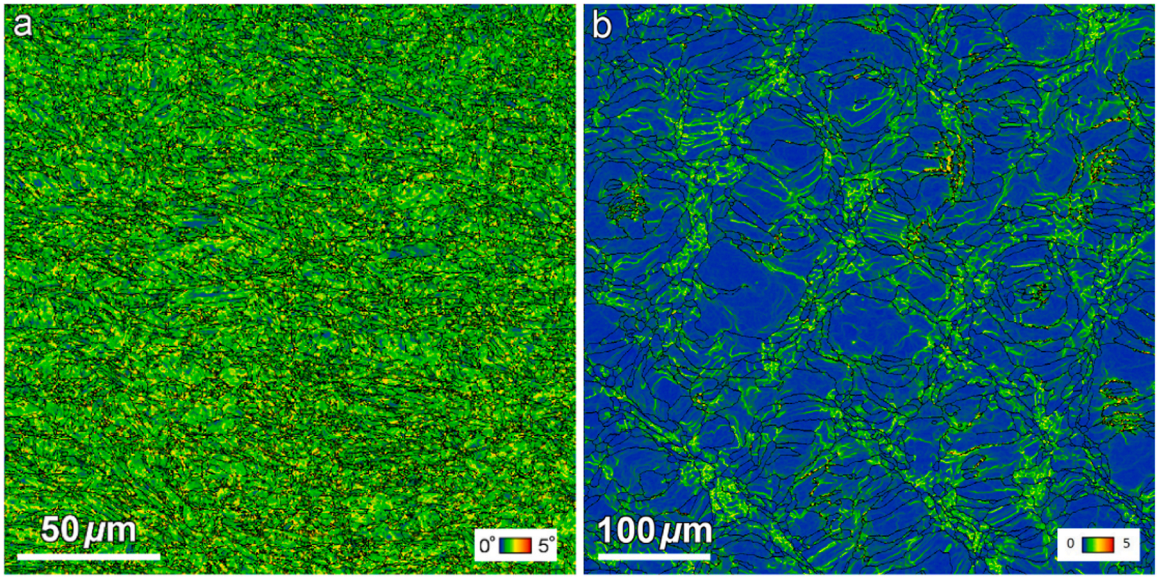

Fig. 12. Kernel average misorientation graphs of the as-printed 17–4 PH stainless steel with (a) martensitic structure (printed with "powder A") and (b) ferritic structure (printed with "powder b").

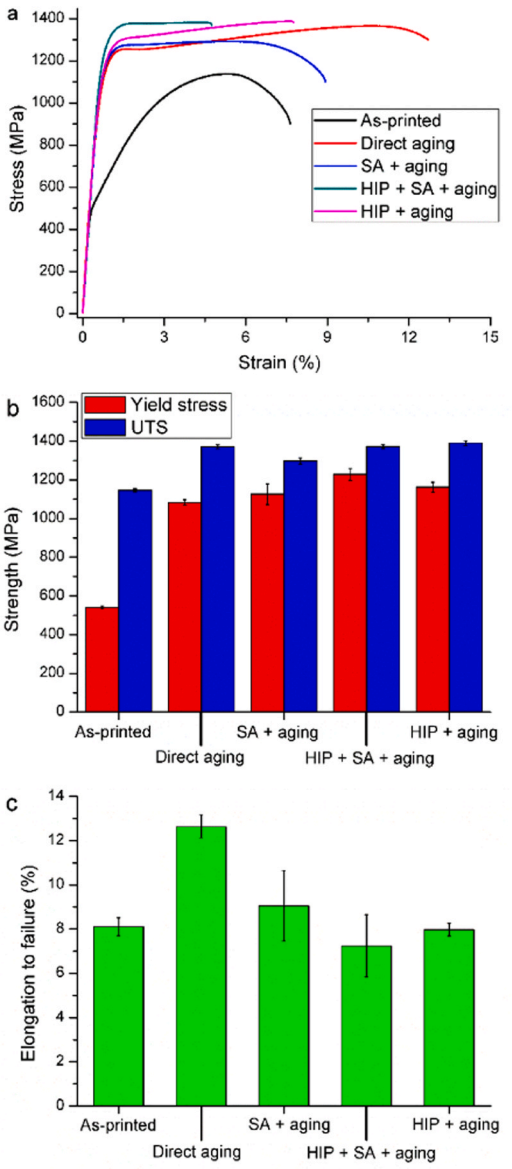

Fig. 13. Typical stress-strain curves (a) along with the yield and ultimate tensile strengths (b) and elongation (c) of the as-printed and post-process heat treated 17–4 PH stainless steel (all sample are fabricated with "powder A").

depicted in Fig. 13. The as-printed specimen exhibits a relatively low yield strength of ~ 500 MPa. The yield strength remarkably increases to 1100 and 1230 MPa after "direct aging" and "HIP + SA + aging" treatments, respectively. The ultimate tensile strength of the post-process heat treated samples is also in the range of 1250–1400 MPa, higher than that of the as-printed component. It should be pointed out that the HIP process has a slightly beneficial influence on the yield strength of the heat treated samples. For instance, the yield strength of the as-printed specimen after direct aging is ~ 1100 MPa that enhances to 1170 MPa at the "HIP + aging" condition. Such improvement can be related to the role of HIP processing on the closure/modification of porosities with irregular shape in the as-printed sample. It is worth to mention that the density of as-printed components was ~ 99.85% which increased to 99.99% after HIP processing. The elongation to failure of heat treated specimens is shown in Fig. 13c. As seen, all the samples, except "direct aged", exhibit an average elongation of 7–9%, while the highest elongation before failure (13%) is achieved after "direct aging" treatment. Considering the microstructure of this sample, such behavior can be well described by the transformation induced plasticity (TRIP)

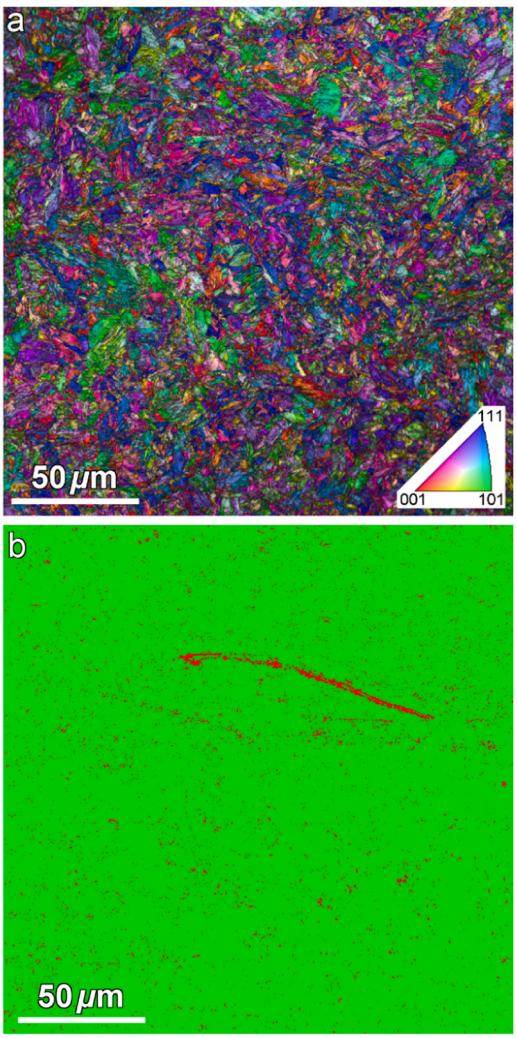

Fig. 14. (a) IQ + IPF and (b) phase map (green color = martensite, red color = austenite) of the "direct aged" specimen after tensile test at a location nearby the rupture point (tension direction from left to right).

effect caused by the high volume fraction of reverted austenite after direct aging [38]. EBSD analysis was carried out (see Fig. 14) at a location nearby the rupture point. The deformed structure consists of mainly martensite with only ~ 2.5 vol% austenite, much reduced from 11 vol% austenite in the un-deformed "direct aged" specimen. It confirms that transformation induced plasticity plays a great role in the increased elongation of direct aged components.

4. Conclusions

In the present investigation, laser powder bed fusion was used to additive manufacture components with two commercial 17–4 PH stainless steel powders of slightly different composition. The as-printed components were subsequently subjected to post-process heat treatments in order to modify the microstructure and achieve improved mechanical properties. The most important findings are as following:

- The microstructure of the as-printed 17–4 PH stainless steel depends highly on the chemical composition of the feedstock powder. A dominant martensitic/ferritic microstructures can be expected after selective laser melting according to the ratio of Cr_{eq}/Ni_{eq} of the melt.
- Increasing the ratio of Cr_{eq}/Ni_{eq} of the feedstock powder leads to higher fraction of δ-ferrite phase in the as-printed condition.

- Different age-hardening responses are observed for the as-printed specimens having martensitic or ferritic microstructures. The ferritic microstructure exhibits a delayed hardening response compared with the martensitic microstructure. The faster hardening response of the martensitic structure can be linked to the higher lattice distortion and dislocation accumulation, resulting in the "dislocation pipe diffusion" mechanism.
- The as-printed 17–4 PH stainless steel with martensitic microstructure is highly susceptible to the formation of reverted austenite during aging treatment, where 19.5% austenite is formed after 15 h direct aging. However, the volume fraction of reverted austenite in the specimen having ferritic microstructure is merely 1.1% after 15 h aging.

CRediT authorship contribution statement

S. Sabooni: Conceptualization, Data curation, Investigation, Methodology, Formal analysis, Writing – original draft, Writing – review & editing. **A. Chabok:** Data curation, Investigation, Validation. **S.C. Feng:** Data curation, Investigation. **H. Blaauw:** Data curation, Investigation. **T.C. Pijper:** Data curation, Investigation, Validation, Writing – review & editing. **H.J. Yang:** Data curation, Investigation. **Y.T. Pei:** Funding acquisition, Conceptualization, Methodology, Formal analysis, Writing – review & editing, Supervision.

Declaration of Competing Interest

The authors declare that they have no known competing financial interests or personal relationships that could have appeared to influence the work reported in this paper.

Acknowledgments

This research was carried out under project number 15808/S16044 in the framework of the Partnership Program of the Materials innovation institute M2i (www.m2i.nl) and the Technology Foundation STW (www.stw.nl), which is part of the Netherlands Organization for Scientific Research (www.nwo.nl). Shaochuan Feng acknowledges Beijing Natural Science Foundation (3214049) and Fundamental Research Funds for the Central Universities, China (QNXM20210026) for financial support.

References

[1] P. Bajaj, A. Hariharan, A. Kini, P. Kürnsteiner, D. Raabe, E.A. Jagle, Steels in additive manufacturing: a review of their microstructure and properties, Mater. Sci. Eng.: A 772 (2020), 138633.
[2] Y. Sun, R.J. Hebert, M. Aindow, Effect of heat treatments on microstructural evolution of additively manufactured and wrought 17-4PH stainless steel, Mater. Des. 156 (2018) 429–440.
[3] Zemin Wang, Xulei Fang, Hui Li, Wenqing Liu, Atom probe tomographic characterization of nanoscale cu-rich precipitates in 17-4 precipitate hardened stainless steel tempered at different temperatures, Microsc. Microanal. 23 (2017) 340–349.
[4] C.N. Hsiao, C.S. Chiou, J.R. Yang, Aging reactions in a 17-4 PH stainless steel, Mater. Chem. Phys. 74 (2002) 134–142.
[5] Hamidreza Riazi, Fakhreddin Ashrafizadeh, Sayed Rahman Hosseini, Reza Ghomashchi, Influence of simultaneous aging and plasma nitriding on fatigue performance of 17-4 PH stainless steel, Mater. Sci. Eng. A 703 (2017) 262–269.
[6] M.S. Shinde, K.M. Ashtankar, Additive manufacturing–assisted conformal cooling channels in mold manufacturing processes, Adv. Mech. Eng. 9 (2017) 1–14.
[7] A. Armillotta, R. Baraggi, S. Fasoli, SLM tooling for die casting with conformal cooling channels, Int. J. Adv. Manuf. Technol. 71 (2014) 573–583.
[8] Amar M. Kamat, Yutao Pei, An analytical method to predict and compensate for residual stress-induced deformation in overhanging regions of internal channels fabricated using powder bed fusion, Addit. Manuf. 29 (2019), 100796.
[9] K.S. Prakash, T. Nancharaih, V.V. Subba Rao, Additive manufacturing techniques in manufacturing - an overview, Mater. Today.: Proc. 5 (2018) 3873–3882.
[10] R. Singh, A. Gupta, O. Tripathi, S. Srivastava, B. Singh, A. Awasthi, S.K. Rajput, P. Sonia, P. Singhal, K.K. Saxena, Powder bed fusion process in additive manufacturing: an overview, Mater. Today.: Proc. 26 (2020) 3058–3070.
[11] L. Zai, Ch Zhang, Y. Wang, W. Guo, D. Wellmann, X. Tong, Y. Tian, Laser powder bed fusion of precipitation-hardened martensitic stainless steels: a review, Metals 10 (2020) 255.
[12] H. Khalid Rafi, Deepankar Pal, Nachiket Patil, Thomas L. Starr, Brent E. Stucker, Microstructure and mechanical behavior of 17-4 precipitation hardenable steel processed by selective laser melting, J. Mater. Eng. Perf. 23 (2014) 4421–4428.
[13] A. Yadollahi, N. Shamsaei, S.M. Thompson, A. Elwany, L. Bian, Effects of building orientation and heat treatment on fatigue behavior of selective laser melted 17-4 PH stainless steel, Int. J. Fatigue 94 (2017) 218–235.
[14] M. Alnajjar, Frederic Christien, Cedric Bosch, Krzysztof Wolski, A comparative study of microstructure and hydrogen embrittlement of selective laser melted and wrought 17–4 PH stainless steel, Mater. Sci. Eng. A 785 (2020), 139363.
[15] M. Alnajjar, F. Christien, K. Wolski, C. Bosch, Evidence of austenite by-passing in a stainless steel obtained from laser melting additive manufacturing, Addit. Manuf. 25 (2019) 187–195.
[16] P.D. Nezhadfar, K. Anderson-Wedge, S.R. Daniewicz, N. Phan, Sh Shao, N. Shamsaei, Improved high cycle fatigue performance of additively manufactured 17-4 PH stainless steel via in-process refining micro-/defect-structure, Addit. Manuf. 36 (2020), 101604.
[17] S. Feng, A.M. Kamat, S. Sabooni, Y. Pei, Experimental and numerical investigation of the origin of surface roughness in laser powder bed fused overhang regions, Virtual Phys. Prototyp. 16 (2021) S66–S84, https://doi.org/10.1080/17452759.2021.1896970.
[18] W. Liu, J. Ma, M. Mazar Atabaki, R. Pillai, B. Kumar, U. Vasudevan, H. Sreshta, R. Kovacevic, Hybrid laser-arc welding of 17-4 PH martensitic stainless steel, Lasers Manuf. Mater. Process. 2 (2015) 74–90.
[19] J.C. Lippold, D.J. Kotecki, Welding metallurgy and weldability of stainless steels, Wiley,, 2005.
[20] M. Shirdel, H. Mirzadeh, M.H. Parsa, Nano/ultrafine grained austenitic stainless steel through the formation and reversion of deformation-induced martensite: mechanisms, microstructures, mechanical properties, and TRIP effect, Mater. Charact. 103 (2015) 150–161.
[21] S. Kou, Solidification and liquation cracking issues in welding, JOM 55 (2003) 37–42.
[22] T.J. Lienert, J.C. Lippold, Improved weldability diagram for pulsed laser welded austenitic stainless steels, Sci. Technol. Weld. Join. 8 (2003) 1–9.
[23] Ch Qiu, M. Al Kindi, A.S. Aladawi, I. Al Hatmi, A comprehensive study on microstructure and tensile behaviour of a selectively laser melted stainless steel, Sci. Rep. 8 (2018) 7785.
[24] P.A. Hooper, Melt pool temperature and cooling rates in laser powder bed fusion, Addit. Manuf. 22 (2018) 548–559.
[25] T. DebRoy, H.L. Wei, J.S. Zuback, T. Mukherjee, J.W. Elmer, J.O. Milewski, A. M. Beese, A. Wilson-Heid, A. Ded, W. Zhang, Additive manufacturing of metallic components – Process, structure and properties, Prog. Mater. Sci. 92 (2018) 112–224.
[26] S. Vunnam, A. Saboo, Ch Sudbrack, T.L. Starr, Effect of powder chemical composition on the as-built microstructure of 17-4 PH stainless steel processed by selective laser melting, Addit. Manuf. 30 (2019), 100876.
[27] L. Couturier, F. De Geuser, M. Descoins, A. Deschamps, Evolution of the microstructure of a 15-5PH martensitic stainless steel during precipitation hardening heat treatment, Mater. Des. 107 (2016) 416–425.
[28] C. Cayron, B. Artaud, L. Briottet, Reconstruction of parent grains from EBSD data, Mater. Charact. 57 (2006) 386–401.
[29] R. Bhambroo, S. Roychowdhury, V. Kain, V.S. Raja, Effect of reverted austenite on mechanical properties of precipitation hardenable 17-4 stainless steel, Mater. Sci. Eng. A 568 (2013) 127–133.
[30] T. LeBrun, T. Nakamoto, K. Horikawa, H. Kobayashi, Effect of retained austenite on subsequent thermal processing and resultant mechanical properties of selective laser melted 17–4 PH stainless steel, Mater. Des. 81 (2015) 44–53.
[31] T.H. Hsu, Y.J. Chang, C.Y. Huang, H.W. Yen, C.P. Chen, K.K. Jen, A.Ch Yeh, Microstructure and property of a selective laser melting process induced oxide dispersion strengthened 17-4 PH stainless steel, J. Alloy. Compd. 803 (2019) 30–41.
[32] Li Wang, Chaofang Dong, Cheng Man, Decheng Kong, Kui Xiao, Xiaogang Li, Enhancing the corrosion resistance of selective laser melted 15-5 PH martensite stainless steel via heat treatment, Corros. Sci. 166 (2020), 108427.
[33] H. Kimura, Precipitation behavior and 2-step aging of 17-4 PH stainless steel, Tetsu-to-Hagane 86 (2000) 343–348.
[34] G. Yeli, M.A. Auger, K. Wilford, G.D.W. Smith, P.A.J. Bagot, M.P. Moody, Sequential nucleation of phases in a 17-4 PH steel: microstructural characterisation and mechanical properties, Acta Mater. 125 (2017) 38–49.
[35] J.B. Ferguson, Benjamin F. Schultz, Dev Venugopalan1, Hugo F. Lopez, Pradeep K. Rohatgi, Kyu Cho, Chang-Soo Kim, On the superposition of strengthening mechanisms in dispersion strengthened alloys and metal-matrix nanocomposites: considerations of stress and energy, Met. Mater. Int. 20 (2014) 375–388.
[36] H. Mirzadeh, A. Najafizadeh, Aging kinetics of 17-4 PH stainless steel, Mater. Chem. Phys. 116 (2009) 119–124.
[37] L.E. Murr, E. Martinez, J. Hernandez, Sh Collins, K.N. Amato, S.M. Gaytan, P. W. Shindo, Microstructures and properties of 17-4 PH stainless steel fabricated by selective laser melting, J. Mater. Res. Technol. 1 (2012) 167–177.
[38] Y.F. Shen, L.N. Qiu, X. Sun, L. Zuo, P.K. Liaw, D. Raabe, Effects of retained austenite volume fraction, morphology, and carbon content on strength and ductility of nanostructured TRIP-assisted steels, Mater. Sci. Eng. A 636 (2015) 551–564.